



LAWRENCE
LIVERMORE
NATIONAL
LABORATORY

UCRL-TR-202620

SPEIR: A Ge Compton Camera

L. Mihailescu, K. M. Vetter, M. T. Burks, E. L. Hull,
W. W. Craig

March 1, 2004

Disclaimer

This document was prepared as an account of work sponsored by an agency of the United States Government. Neither the United States Government nor the University of California nor any of their employees, makes any warranty, express or implied, or assumes any legal liability or responsibility for the accuracy, completeness, or usefulness of any information, apparatus, product, or process disclosed, or represents that its use would not infringe privately owned rights. Reference herein to any specific commercial product, process, or service by trade name, trademark, manufacturer, or otherwise, does not necessarily constitute or imply its endorsement, recommendation, or favoring by the United States Government or the University of California. The views and opinions of authors expressed herein do not necessarily state or reflect those of the United States Government or the University of California, and shall not be used for advertising or product endorsement purposes.

This work was performed under the auspices of the U.S. Department of Energy by University of California, Lawrence Livermore National Laboratory under Contract W-7405-Eng-48.

SPEIR: a Ge Compton camera

L. Mihailescu^{a 1}, K.M. Vetter^a, M.T. Burks^a, E.L. Hull^a,
W.W. Craig^a,

^a *Lawrence Livermore National Laboratory, Livermore, USA*

Abstract

The *SPEctroscopic Imager for γ -Rays* (SPEIR) is a new concept of a compact γ -ray imaging system of high efficiency and spectroscopic resolution with a 4π field-of-view. The system behind this concept employs double-sided segmented planar Ge detectors accompanied by the use of list-mode photon reconstruction methods to create a sensitive, compact Compton scatter camera.

PACS: 29.40.Gx 42.30.W 29.85.+c 95.55.Ka 87.59.-e

Key words: Compton camera; HPGe detectors; gamma-ray tracking; gamma-ray imaging; Compton scattering

1 Introduction

Imaging γ -rays efficiently and accurately remains an objective in many applications involving radioactive elements, such as biomedical imaging, γ -ray astrophysics, nuclear non-proliferation or environmental monitoring. The predominance of the Compton scattering process for photons of energies ranging from 150keV to 4MeV results in a diffuse release of energy in any material, so that collimator-based imagers, such as Anger cameras or coded-aperture cameras could only provide a poor estimate of the photon initial direction, especially at increased energies.

A compact, high efficiency, high resolution γ -ray imager can be obtained by using the properties of the most dominant interaction process in this energy

¹ Corresponding author. Tel: +1-925-4221101; Fax: +1-925-4230238; E-mail: mihailescu1@llnl.gov

range, the Compton scattering process. This is the Compton scatter camera [1]. Since there is no intervening collimator or mask in which the γ -rays can be stopped, Compton scatter camera claims an advantage in its much superior sensitivity over the collimator-based imagers (Anger cameras, pinhole cameras or coded apertures). Compared with the standard collimator based cameras, the gain in detection sensitivity of such a Compton camera would be 2 to 3 orders of magnitude, depending on the photon energy. Another advantage of a Compton camera is that, unlike the collimator based imagers, it can be reliably used for objects situated both in far field, as well as for near field objects, covering a field of view which can be as large as 4π . Imaging systems based on the Compton scatter camera approach were proposed decades ago [1,2], however, no compact, functional system has been made. This is due to the lack of suitable detectors. The reason for this is not hard to understand. On the one hand, for reasons of efficiency, such a detector should be of high density and as large as possible, on the other hand, to be able to differentiate the multiple interactions of the gamma-rays within the detection material, a high granularity of detection and a low Z material is required. A light, low Z material would also maximize the predominance of the Compton effect. These are contradictory requirements which, for optimum results, would favor a very large, low Z detector, with hundreds of thousands of detection elements each covering a maximum volume of about 10 mm^3 . Technically, the creation of such a device has not been possible, since all these detection elements (segments) require high resolution read-out channels. The large number of channels needed would require a large physical space contributing to an increase of insensitive material in the detection space. A large number of channels would also contribute to a large power consumption, creating heating problems for the detectors. In addition, if semiconductor detectors are considered, the existence of a high density of electrode segments will increase the chance for charge splitting and incomplete charge collection, degrading the spectroscopic performances. All these unwanted effects would finally ruin (and in fact have ruined) the usefulness of such a detection system as a γ -ray imager.

Most of the Compton scatter cameras proposed [3] or built [3–5] to date, employ at least two layers of position sensitive detectors, one of which acts as a *scatterer*, in which the γ -ray is supposed to release part of its energy in a Compton scattering, the other as an *absorber*, in which the down-scattered photon is fully absorbed in a photoelectric effect. By optimizing the geometrical arrangement of the absorber (A) in respect to the scatterer (S), and by choosing a lighter detection material as the scatterer and a heavier detection material as the absorber, the probability of having a scattering in S followed by an absorption in A is increased. However, in many cases, the background produced by the photons that do not follow this scenario can be overwhelming, unless the sequence of the interactions can be determined from the time of their occurrence [5]. This time-of-flight approach requires an increased distance between S and A to allow for the photon time-of-flight to be larger than

the detector time resolution. An increased distance however, leads toward a decreased detection sensitivity. This was the main factor limiting the efficiency of the largest Compton scatter imager built to date, the Comptel telescope [5].

The alternative to using a scatterer-absorber Compton camera system is to employ a monolithic position sensitive detector that acts as a scatterer and absorber at the same time. This is the approach we follow in the present work, in which we employ large, double-sided segmented planar Germanium (Ge) detectors [6], in a compact Compton camera system that we call the *SPEctroscopic Imager for γ -Rays (SPEIR)*. The advantage of this approach consists in the potentially superior imaging sensitivity, system compactness, and large field-of-view. The disadvantages relate to the requirement to unambiguously determine the scattering sequence of the γ -ray in the monolithic detector, by which the position of the first interaction, \vec{r}_1 , and the direction of the down-scattered photon after the first interaction, \vec{s}_{12} , can be made available. These two vectors together with the scattering angle, θ , and the energy of the incident photon, E_0 , constitute the data needed to reconstruct γ -ray images in a Compton camera imager. As it will be explained below, the demand for these data calls for an increased detection granularity and position resolution on the top of a high energy resolution. In the recent years, new high performance digital electronics and position sensitive semiconductor detector technologies have become available, creating the foundation for the present approach. In particular, the double-sided segmented planar Ge detectors with blocking contacts using the amorphous Ge technology [7] have shown to be reliable, with small insensitive volumes, providing very good spectroscopic performances.

In the next section, the imaging concept behind SPEIR will be introduced along with the basic factors affecting the imaging performance of the system. In section 3, the Ge detector and data acquisition system will be described. While some basic justifications for the data processing approach will be mentioned in this section, a more thorough understanding of the system will be apparent in section 4, where each data processing step in the analysis chain will be described. The experimental results of each processing step will be compared to the expected data as resulting from Monte Carlo simulations and calculations, when possible. Since the novelty of the approach consists mainly in the employed analysis, the main emphasis will be put on section 4. This section will also discuss the imaging capabilities of the system. From the perspective offered by the present imaging and sensitivity performances, possible applications based on the SPEIR concept will be discussed.

2 Compton imaging with SPEIR

As already mentioned in the introduction, SPEIR system does not rely on the classical Compton camera arrangement formed by a scatterer-absorber assembly, but rather on a monolithic detector, in this case a double sided segmented planar Ge, which acts as a scatterer and absorber at the same time. Figure 1 shows a schematic spatial view of a planar Ge detector with orthogonal strips acting as a Compton camera. The color (shades of gray) coded dots represent typical gamma-ray interaction points occurring in the detector volume as produced by three different photons. Each color (shade) is associated to a different photon. The corresponding cones which have their tips on the point of the first Compton interaction for each incident photon, are virtual surfaces formed by all possible directions of the incident γ -photon. The opening angle of the cones is determined by the scattering angle of the incident γ -ray, θ , and their symmetry axes by the scattering directions, \vec{r}_{12} . The notations associated with a typical γ -ray event can be better identified in figure 2. Having measured the positions and energies of all interactions, the scattering angle θ is calculated using the Compton scattering formula (equation 1), and the scattering direction is determined by the relative positions of the first and second interactions $\vec{r}_{12} = \vec{r}_2 - \vec{r}_1$. By acquiring many such events, the distribution of the source is found by analyzing the statistics of the cone intersections in the image space. For this purpose, image reconstruction methods similar to the one used in tomographic problems, analytical or iterative, are employed.

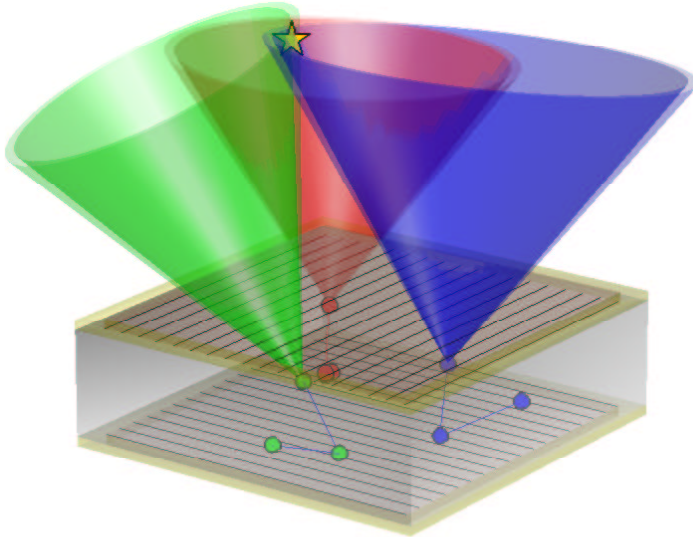


Fig. 1. Representation of a single double-sided segmented Ge detector acting as a compact Compton camera

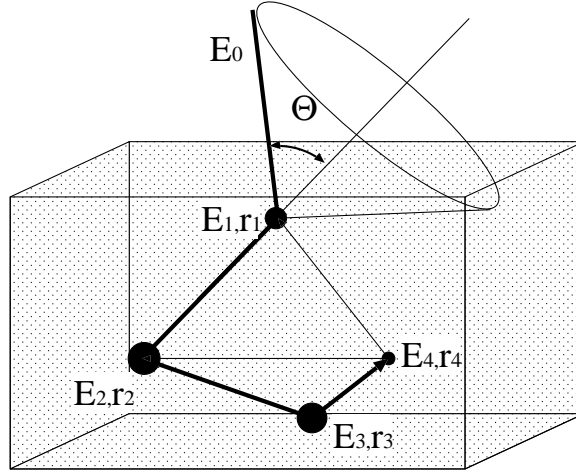


Fig. 2. Representation of a γ -ray event occurring in a compact Ge Compton camera

Depending on the particular imaging application, two general scenarios emerge. The first case is when sources are situated at large distances from the detector as compared to the geometrical extend of the detector. This is the so-called *far-field approximation*. Gamma-ray astronomy and nuclear non-proliferation are two representative applications in this category. The second case, *near-field*, is when the sources, usually highly distributed, are found in close proximity. Most bio-medical investigations using radioactive tracers are part of this category. For each of these two categories, separate discussions will be made in what regards the optimization of the imager geometry and the image reconstruction algorithms, in particular.

For increased detection efficiency, two or more detectors can be assembled in close proximity, however, the analysis of the data is conducted as if it was a single monolithic detector. By not having restrains on the order of the interactions in the detection system, this approach provides a maximum use of the detected photons for imaging, ensuring at the same time a large field-of-view. The advantage brought upon the increased sensitivity by the use of a compact, monolithic detector assembly, comes up with the disadvantage of a decreased average distance between consecutive individual interactions. This reduced distance leads towards an increased total angular uncertainty. As noticed from equ. 6 below, the only way to compensate for this effect is to pursue an improved position resolution of detection.

Following the description of the above mentioned imaging procedure, two important requirements for the imaging system become evident: the detector must have the capability to identify and decompose multiple interactions, and, based on that, the scattering sequence of the γ -ray in the detector must be determined. The solutions we have investigated for these two problems are described in the next sections.

Before describing in detail the hardware components of the SPEIR system and the associated data analysis methods, a few paragraphs are in order to describe the factors contributing to the final performance of the system, in particular the attainable *angular uncertainty*, and the capability of the system to decompose multiple interactions, capability represented by the *detector granularity*.

2.1 Angular uncertainty

Common to all Compton scatter imagers, the Compton scattering formula is used to extract information about the direction of impinging γ -ray photons:

$$\cos \theta = 1 + \frac{1}{A_0} - \frac{1}{A_d} \quad (1)$$

θ is the scattering angle of a photon in a Compton interaction, $A_d = (E_0 - E_1)/(m_e c^2)$, $A_0 = E_0/(m_e c^2)$, in which E_0 is the energy of the incident photon, normally obtained by summing the deposited energies of all interactions in the detector, and E_1 is the amount of energy deposited in the first Compton interaction. m_e is the rest mass of the electron, and c is the speed of light.

The uncertainty in the calculation of $\cos \theta$ is easily obtained from equ. 1 by propagating the incertitude in the deposited energies:

$$\delta^2 \cos \theta_E = \frac{1}{A_0^4} \delta^2 A_0 + \frac{1}{A_d^4} \delta^2 A_d \quad (2)$$

The subscript E in $\delta^2 \cos \theta_E$ is meant to indicate that the $\delta \cos \theta$ error component accounts only for the incertitude in energy. It should be mentioned that the δA_0 component is not necessarily the same as δA_d . Whereas δA_0 accounts for the cumulated errors for all interactions as determined by the finite detector energy resolution, δA_d contains both the above mentioned errors, and the incertitude in the energy deposited in the first Compton interaction introduced by the unknown angular momentum of the electron on its orbital movement inside the Ge atoms at the moment of interaction with the photon [8,9].

The incertitude in the scattering angle, θ , can be further modified to include the component determined by the incertitude in the scattering direction:

$$\delta \cos \theta = (\delta^2 \cos \theta_E + \delta^2 \cos \theta_r)^{1/2} \quad (3)$$

The last term, $\delta \cos \theta_r$, contains the error in the scattering direction as reflected in the cosine of the scattering angle, θ . It can be expressed as:

$$\delta^2 \cos \theta_r = \sin^2 \theta \delta^2 \theta_r \quad (4)$$

Assuming identical position resolutions for all three physical coordinates, $\delta x = \delta y = \delta z = \delta r$, the incertitude in the scattering direction $\delta \phi$ that can be transferred to the scattering angle incertitude, $\delta \theta_r$, is:

$$\delta^2 \theta_r = \delta^2 \phi = \sin^2 \theta \delta \phi = \frac{2\delta^2 r}{r_{12}^2} \quad (5)$$

where r_{12} is the distance between the first Compton scattering and the next interaction. This finally leads to:

$$\delta^2 \cos \theta_r = 2(1 - \cos^2 \theta) \frac{\delta^2 r}{r_{12}^2} \quad (6)$$

While the position and energy resolution of detection can theoretically be improved for a better final angular resolution through technical developments, it is the Compton profile that is the fundamental limit in the attainable angular resolution with a Compton camera. The only way to deal with this is either chose a detector material in which the Doppler broadening is minimal, or just try to deconvolve for this effect in the final γ -ray image. Among the other detection materials, Ge has a moderate Doppler broadening, larger for example than Si, but smaller than CdZnTe [10,11].

2.2 Detector granularity

The finite size of the electrode segments will affect the capability of the system to identify interactions occurring within the same detection element (the detector volume whose charge carriers produced within are collected by the same electrode segment). To characterize this detection feature we introduce a new parameter, the *detector granularity*. This is an important parameter which will affect the performance of the imager. We define *granularity* $g(E_0)$ as the relative linear dimension of a “granule” ξ , as compared with the total attenuation length or the mean free path $L(E_0)$ of a γ -ray photon of energy E_0 in a particular detection material. A “granule” is the volume within a detector inside which two separate interactions cannot be distinguished nor decomposed. For an unsegmented, non-position sensitive detector the granule

is the detector itself. The *granularity* can be calculated as:

$$g(E_0) = \frac{\xi}{L(E_0)} \quad (7)$$

where the attenuation length of a photon $L(E_0)$ is:

$$L(E_0) = \frac{1}{\mu(E_0)} = \frac{1}{\rho N_A (Z/A) {}_e\mu(E_0)} \quad (8)$$

Here, $\mu(E_0)$ is the absorption coefficient, ρ is the density of the detection material, Z is its atomic number, A is its atomic weight, N_A is the Avogadro's number, and ${}_e\mu(E_0)$ is the absorption coefficient, or the cross section per electron for a photon of energy E_0 . Since ${}_e\mu(E_0)$ stays about the same for all elements, a generic, approximate value for granularity, independent of the photon energy can be defined as:

$$g = \xi \rho \frac{Z}{A} \mu_0 \quad (9)$$

Here, $\mu_0 = {}_e\mu(E_0)N_A$ by convention can be taken as a constant by setting $E_0 = m_e c^2 = 511 \text{keV}$. Assuming the value for the total absorption coefficient per electron of ${}_e\mu(511 \text{keV}) = 2.866 \cdot 10^{-25} \text{cm}^2$ [12], the absorption coefficient per mole at $E_0 = 511 \text{keV}$ becomes: $\mu_0 = 0.17259 \text{cm}^2$. For the case when the dimensions of the “granule” are different for the three spatial coordinates, the granularity can be represented as a three-dimensional vector: $\vec{g} = 0.173 \cdot \vec{\xi} [\text{cm}] \rho [\text{cm}^{-3}] Z/A$.

A finer detection granularity helps to increase the fraction of detected events whose interactions are correctly identified, by a better differentiation of multiple interactions occurring in close proximity. This will increase the chance for a correct identification of the scattering sequence in the subsequent analysis, finally decreasing the image background associated with the misreconstructed photons, i.e. a better image contrast is achieved. In the same time, identifying the presence of two interactions in close proximity as opposed to having the two interactions misinterpreted as a single interaction, will help for a better definition of the scattering direction, contributing to a better definition of the scattering angle, i.e. a better image resolution is achieved. The most effective way to estimate quantitative relationship between the detector granularity and the image contrast and resolution is by performing Monte Carlo simulations. For this purpose, the GEANT4 library [13] is used in this work. In a first approximation, the fraction of events without more than one interaction in the same granule decreases exponentially with g :

$$F = K e^{-g} \quad (10)$$

The proportionality factor K includes the dependency on the average energy of the down-scattered photon following a Compton interaction.

The best detector design would call for the finest granularity possible, if the path of the photoelectron through the detector material is disregarded. In practical terms, however, a “granule” size smaller than the path of an electron produced in an interaction would not be of much help, since this would also contribute to inadvertently divide a single interaction in two or more components. Certainly, the components could be added back to reconstruct the path of the photoelectron, but this would also result in a decreased total energy resolution due to the quadratically addition of the individual energy uncertainties. Alternatively, if the granularity could achieve such high values so that the path of the photoelectrons could be imaged by observing the granules which are hit, this could theoretically be used to determine the transferred momentum to the electron in a Compton interaction, helping to reconstruct the 4-vector of the incident γ -ray. This approach for γ -ray imaging, however, is not addressed in this paper, mainly because of the very demanding detector requirements for energy resolution and granularity, to which no practical technical solution are available at this time.

If the detection granularity is achieved through the segmentation of the electrodes exclusively, the limit in granularity will be determined by the practical size and number of segments. For example, for a Ge detector of a total volume of $20 \times 80 \times 80 \text{ mm}^3 = 128000 \text{ mm}^3$, granules of $2 \times 2 \times 2 \text{ mm}^3$ would require 16000 segments. The same number of high resolution read-out channels would be involved, which is very often a prohibitive practical solution. An alternative answer to this problem is to employ analysis methods able to extract supplementary information from the signal waveforms, leading to an increased position resolution and a finer granularity than the ones provided by the segmentation alone. This is the solution employed in the present work.

For event rates of detection of up to about $2 \cdot 10^6 \text{ cps}$, individual events can be easily discriminated in time, and therefore, unlike in nuclear physics problems [14], separating interactions according to the incident photons from which they are produced does not constitute an issue.

3 Instrument description

3.1 Ge detectors

The use of semiconductors, especially high purity monocrystals of germanium cooled to liquid nitrogen temperature, have provided the optimum energy

resolution and detection efficiency in high resolution γ -ray spectroscopy. Ge detectors are a good choice for a Compton camera, not only because of the energy resolution, but also because they can be made very large, providing a good detection efficiency.

A breakthrough in the detector technology was the introduction of the planar Ge detectors using the amorphous Ge contact technology [7]. This technology has replaced the standard Boron implanted n+ contacts and the difficult to segment Lithium diffused p+ contacts, so that high levels of electrode segmentation became reliable, leading toward new, unprecedented levels of position resolution and detection granularity with Ge detectors. As discussed earlier, both parameters are very important in a compact Compton camera. Besides, Ge has a conveniently high Compton scattering cross section for a large range of γ -ray energies [12], and a relatively low Doppler broadening of the scattered γ -rays determined by the Compton profile in Ge [10].

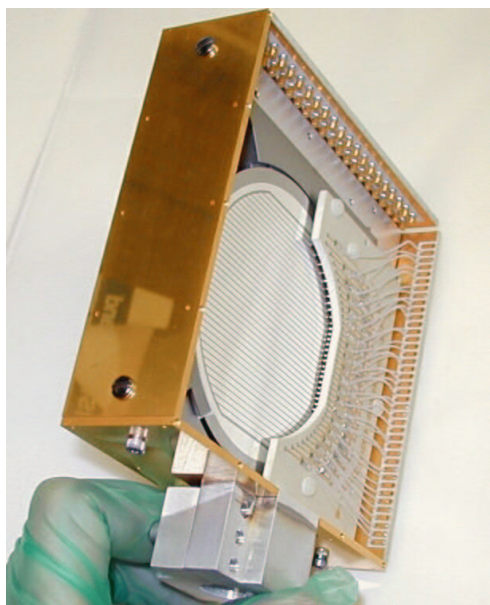


Fig. 3. Picture of the planar Ge detector with orthogonal strips inside the cryostat

The results reported in this paper were obtained using two planar Ge detectors with orthogonal segments of different geometries (NN-1 and NN-2). The crystal of the NN-1 detector has a circular shape, of a diameter of 70mm, and 11mm thickness [6]. The surface leakage currents are drained by guard rings of about 5mm thickness around both electrode edges. The 19 segments on each electrode have a pitch size of 2mm, with a 0.5mm gap between each other. The second detector, NN-2, has a circular shape with a diameter of 100mm. The detector active area covers a square-like shape with rounded corners (see fig. 3). The dimension of the active area is 76mm from side to side. The detector has a thickness of 11mm with guard-rings around each electrode of variable thicknesses between 2.3 to 5.9mm. The 38 segments on each electrode have a pitch size of 2mm, with a 0.5mm gap between each other. The measured

detector noise was 1.0keV for detector NN-1, and 1.2keV for detector NN-2 at a peaking time of $4\mu\text{s}$. The bias voltage used for both detectors was 300V.

Since there are strong limitations on the segmentation level that can be made, limitations especially determined by the maximum number of high resolution channels that can be reliably and practically read, the use of high-resolution Ge detectors for γ -ray position sensitivity calls for a segmentation scheme involving double-sided orthogonal segments instead of pixilated ones. This, however, reduces the detection granularity that we attempt to partially recover in the subsequent data analysis. By digitally analyzing the pulse shapes of the detector segment signals, a position resolution superior to the one provided by the segmentation alone can be achieved. However, this approach requires a data acquisition system that preserves the large bandwidth of the signals.

3.2 Electronics for Data Acquisition

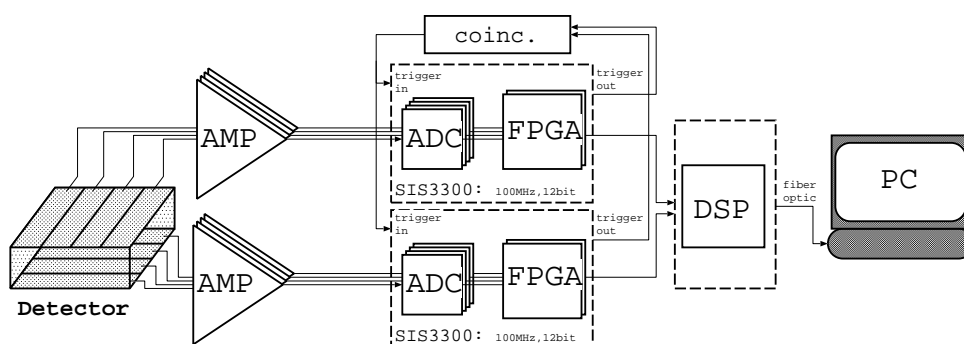


Fig. 4. Schematics of the SPEIR data acquisition

Figure 4 provides a simplified representation of the data acquisition system. The first elements in the data acquisition are the charge sensitive preamplifiers. They have a relatively large bandwidth transfer function, corresponding to an impulse response function of 15ns rising time at 8pF input capacity.

The subsequent filtering and data acquisition and analysis is done exclusively in the digital domain. For digitization and filtering we use the commercial Struck Innovative Systems' SIS3300 VME digitizer/transient recorder that has a sampling rate of up to 100MHz and 12 bit resolution. Each board accommodates 8 channels, an FPGA is used to handle the digitized data for every two channels, allowing for much of the digital filtering and processing to be done on the fly. The analog bandwidth of the digitizers fits well the preamplifier bandwidth. For synchronous use of all the digitizing boards, an external clock can be used.

Analog trigger signals produced by each channel are collected into an external coincidence module. The coincidence module requires at least two trigger

signals, one from each of the detector electrodes, to make a first selection of viable events. Once the event is declared valid, a VME card collects the data from the firing channels and stores them into a FIFO. When the FIFO gets filled, the data are transferred with a data rate of 40MB/sec through fiber optic to a PCI interface. Here the data can be either real-time analyzed on the PC or stored directly into the hard memory.

3.3 Ancillaries

A 360° lens photo-camera was used in conjunction with the SPEIR system for a visual identification of γ -ray sources. The TotalViewTM panoramic photolenses were mounted on a 4500 Coolpix Nikon digital camera. The proprietary TotalViewTM software creates the panoramic optical images. These images can be loaded in the SPEIR data analysis system, so that the contour plot of the γ -ray image can be superposed over the visual image. This assembly can constitute the basis for a future, deployable system for applications involving the surveillance of radioactive materials.

4 Data Analysis

The data analysis chain contains the steps needed to bring the data from the level of detector signal waveforms to the final map of γ -ray sources. Due to the finite granularity, position resolution and energy resolution, not all photons Compton scattered and subsequently absorbed in the detector will be of use to image the γ -ray source. The purpose of the developed data analysis is to extract the most information available from most detected photons.

Table 1

Data Analysis Chain and the resulting data after each step (Acronyms for the modules: *ADC*: Flash Analog-to-Digital Converter on the acquisition card, *FPGA*: Field Programmable Gate Array on the acquisition card, *DSP*: Digital Signal Processor on the VME read-out card, *PC*: Personal Computer).

| Step | Method involved | Module | Resulting Data |
|------|-------------------------------|---------|--|
| 1 | Digitization (hardware) | ADCs | Signal waveforms |
| 2 | Pulse Shape Analysis | FPGAs | List of firing segments (E_{ij} , t_{ij} , a_{ij}) |
| 3 | Comprehensive Event Selection | DSPs/PC | List of interactions, (E_{ik} , r_{ik}) |
| 4 | Gamma-ray Tracking | PC | Scattering parameters (θ_i , s_i , r_i) |
| 5 | Image Reconstruction | PC | γ -ray image (M) |

An enumeration of the analysis steps, their corresponding place of implementation and the data which results at each step is shown in table 1. Each analysis step takes as input the data provided in the precedent step. The first analysis step *Pulse Shape Analysis*, contains a set of filters and procedures used to provide the basic parameters used to identify and characterize the interactions. Among these basic parameters are the energies and timings of the signal pulses. The PSA procedures take as input the raw signal waveforms, and since they act at the channel level, without need of data from other channels, they can be implemented on the first processing stages, namely, the FPGAs on the acquisition boards. The next *Comprehensive Event Selection* uses the data from the channels with induced signals to determine the positions \vec{r}_{ik} and energies E_{ik} of all interactions which can be decomposed, within the limit given by the detector segmentation. Here, k is an index over the interactions corresponding to a photon i . Since this procedure requires information from all channels, it can be implemented either on the ADCs on the VME acquisition card, or on the PC Workstation, or it can be split between the both. The objective of these two processing steps is to disentangle multiple interactions occurring in the same or adjacent segments, as well as to interpolate their position to a precision superior to that provided by the segmentation alone. In this way, an effective granularity corresponding to $11 * N^2$ detection elements should be obtained by using in fact only $(2*N/3)$ actual elements (N is the number of segments per coordinate). Besides the obvious advantage of the huge reduction in the number of read-out channels, other advantages of such an approach are that less charge splitting between segments will occur, and the charge carriers are collected more efficiently.

For each detected photon, the resulting list of interactions is fed into a *Gamma-Ray Tracking* algorithm which determines the most probable scattering sequence of the γ -ray inside the detector. After this procedure, three scattering parameters are saved: the scattering angle, θ_i , the position of the first Compton interaction vertex, \vec{r}_i , and the scattering direction, \vec{s}_i . The last data analysis step, the *Image Reconstruction*, uses the scattering parameters of all selected photons to reconstruct the spatial distribution of the γ -ray sources.

4.1 *Pulse Shape Analysis (PSA)*

The *Pulse Shape Analysis* module contains a collection of digital filters applied on the raw digitized signal waveforms of each segment for the extraction of the: 1.) trigger to identify segments with deposited energy, 2.) time stamp of the 50% threshold, 3.) deposited energy, 4.) transient amplitude. The four parameters are used for, sequentially: - identify the occurrence of an event, - pairing the segments on opposite sides to identify individual interactions, - determining the energies of the individual interactions, - determining the depth

of interaction for each interaction, - interpolating the positions of interactions within the segment's width. Many of these processes take place in the next module, the *Comprehensive Event Selection*. In what follows, the extraction of the above mentioned parameters is described.

The filter for *signal triggering* uses a digital version of a trapezoidal filter with a delay line time of 500ns, and a peaking time of 300ns. The trigger signal is transferred to a coincidence module, which requires at least one segment firing from each electrode. The output signal from the coincidence module is read by the SIS3300 modules, signaling the occurrence of a possible viable event.

The filtering for *energy* determination uses the trapezoidal based Moving Window Deconvolution digital algorithm described in [15]. The integration time was $5\mu\text{sec}$.

A *timing* algorithm finds the 50% of the pulse amplitude with sub-sampling interval resolution. There are two versions of filters used for timing. The first uses a digital version of the Constant Fraction Discriminator (CFD) method, with a 30nsec delay time and a fraction of 50%. For sub-sampling interval resolution, a linear interpolation is performed to identify the zero crossing. The second filter is specifically designed for the digital environment. Instead of a constant fraction, it uses the total pulse amplitude to find the 50% crossing. Since the total amplitude can be very accurately determined using the energy filter, this approach eliminates some of the noise associated with the cumulated differential noise which exists when two signals are subtracted in the CFD.

The timing at 50% of the pulse amplitude in a segmented planar Ge detector is very close to the point of the steepest slope, where the best time resolution can be achieved. This fraction is of much more interest however, because it indicates the moment the charge carriers formed in an interaction arrive to the detector electrodes. The reason for that is that the largest induced electric current in the electrodes is proportional to the weighting fields, \vec{E}_w , of the collecting electrode, $I(t) = e\vec{v}_e(t)\vec{E}_w$ (e is the electric charge of the carriers, $\vec{v}_e(t)$ is their drift velocity), and because of the small dimension of the electrodes as compared with the detector thickness, the highest values for the weighting fields take place in the close proximity to the electrode. Since the charge signal is an integral over the current $Q(t) = \int_{-\infty}^t I(t)dt$, the largest variation takes place when the current is largest.

Once the time of arrival for electrons and holes is known, from the time difference one can deduce the relative drift time, and through that, the depth of interaction. Since the electric fields inside the planar detector are close to the saturation in the drift velocity for both electrons and holes, one can assume constant drift velocities for the charge carriers, so a linear relation can be approximated between the depth of interaction, z , and the difference in

collection times:

$$z = z_0 + k_z \cdot (t_e - t_h) \quad (11)$$

t_e is the time when the electrons arrive to the electrode, t_h is the time when the holes arrive to the electrode, z_0 is a constant which is close to the halfway between the detector electrodes, the displacement from which is due to the difference in the saturated drift velocities between holes and electrons, k_z is a proportionality factor. In our case, we used $z_0 = 5.2mm$, $k_z = 0.04mm/ns$.

The depth of interaction is the first component obtained to increase the position resolution of detection by using the analysis of the signal waveforms. Several previous works have used this concept to obtain the depth of interaction [16]. In addition, in the present work we pursue an increased position resolution in the other two coordinates by analyzing the signal waveforms. The physical property which allows for interpolating positions within the segment's borders is the fact that the amplitude of the transient signals induced in segments adjacent to the collecting segment falls approximately exponentially with the distance to their borders. Therefore, by observing the difference in the maximum amplitude of the transient signals in the two adjacent segments, information can be obtained about the position of the interaction relative to the segments border. This requires a new filter which extracts the amplitude of the transient signals in adjacent segments synchronous in time with the 50% crossing of the pulse in the collecting segments. A moving average filter with a time constant of 30ns was used to cut-off some of the high-frequency noise. Once having measured the two amplitudes $A_{s-1}(t50_s)$ and $A_{s+1}(t50_s)$, a normalized ratio, R is calculated:

$$R = \frac{A_{s+1}(t50_s) - A_{s-1}(t50_s)}{A_{s+1}(t50_s) + A_{s-1}(t50_s)} \quad (12)$$

from which the interpolated positions are obtained for the x coordinate:

$$x = x_s + k_x \cdot R \quad (13)$$

Similarly for the y coordinate:

$$y = y_s + k_y \cdot R. \quad (14)$$

Here, x_s and y_s are the coordinates of the collecting segments. An example showing the capability for position interpolation is represented in fig. 5. A ^{57}Co source was employed to irradiate the surface of the Ge detector NN-1. A hole collimator was interposed to cast a shadow on the detector surface. Using the

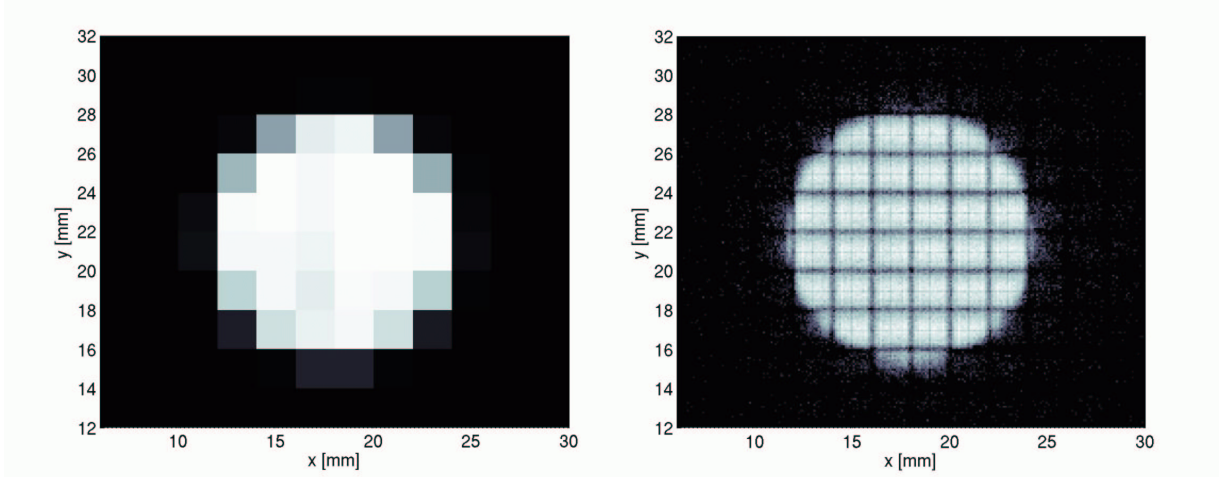


Fig. 5. Shadow of a hole on the detector surface. Left: no position interpolation used; right: with position interpolation.

same measured data, the left picture shows the shadow as obtained without using interpolation, the right picture shows the shadow using the above described Pulse Shape Analysis. One can note in the right picture a grid of lower intensity corresponding to the gaps between segments. The reason for this is that many of the interactions occurring within these gaps produce charge carriers which are collected by two adjacent electrodes (charge split events), which we chose not to include in the image. In a separate measurement, using a $200\mu\text{m}$ pinhole collimator in the front of a ^{57}Co source, we measured an average position resolution of $440\mu\text{m}$ at 122keV . It should be mentioned that in order to have accurate readings of the timing and transient amplitudes, the noise should be kept as low as possible at the higher band of the frequency spectrum, using in the same time read-out channels with a bandwidth extending to about 40MHz .

Besides increasing the position resolution, an analysis of the signal waveforms can be also used to increase granularity by decomposing interactions occurring in the same segments. This can take place by combining the information from segments from opposite electrodes, and identifying the cases where two or more interactions which took place in two or more different segments of a detector side, took place in the same segment on the other side. A further reduction in granularity can take place by identifying two or more charge deposition components in the waveform of a single segment. This would help identify two interactions occurring at different depths, but in the same segment on one side and the other of the detector.

In the present development phase, all these filters are implemented real-time on the workstation. However, once the algorithms will be optimized, they will be implemented on the FPGAs of the SIS3300 cards. At that time, the data transfer load to the workstation will be much reduced, ensuring a much higher

event rate capability.

4.2 *Comprehensive Event Selection (CES)*

The purpose of this analysis module is two folded:

- 1.) Make use of the most detected photons for imaging by: a.) combining segments from opposite sides to reconstruct interactions, and b.) decompose multiple interactions occurring in the same segments to increase the effective detector granularity.
- 2.) Then, select only the events with a good chance to contain interactions which are correctly identified. For that, an event figure-of-merit FoM_{CES} is calculated to assess the usefulness of the event for imaging.

In its pursue of decomposing and identifying interactions, the *Comprehensive Event Selection* algorithm contains several successive steps:

- 1.) Compare the total energy from the two detector electrodes, reject the events which have differences in the total energy larger than the expected detector resolution
- 2.) Check-out for events showing single interactions, and reject them, since no Compton imaging is possible.
- 3.) Check the deposited energy from individual channels on opposite sides, and determine the opposite segments which have the most similar energy. If the difference in the energies of any two opposite segments is smaller than the detector resolution, accept the paired segments as fired by the same interaction, then increment the total number of interactions for the current event, and determine the interactions parameters. Subtract from the initial data the paired segments. Step 3.) is repeated until no pairing is possible.
- 4.) Out of the segments left unpaired, add the energies of any two of them on any one side and compare the resulting energy to the energies of individual segments on the other side. If the smallest energy difference is below the expected detector resolution, accept the pairing as either determined by 2 interactions hitting two segments on one side and one on the other, or a single interaction whose charges were collected by two adjacent electrodes on one side (charge splitting interaction). An indication for a charge splitting is if the two segments on one side are adjacent, and if the timing for the two channels is smaller than the time resolution. The similar timing would indicate the same depth of interaction for the two components, and if the probability of having the gamma-ray scattering within that small distance is smaller than

the probability of charge splitting, a single interaction is assumed, otherwise two interactions are decomposed and identified.

5.) Similarly to step 4.), try to combine 3 or more segments on one side with single segments on the other to identify interactions.

The factors contributing to the calculation of the figure of merit of this analysis FoM_{CES} , are: the physical separation of the interactions, the presence of a charge split interaction, the number of multiple interactions per segment. Depending on the purpose of each particular γ -ray imaging application, the threshold in FoM_{CES} can be changed to provide the best trade-off between sensitivity and contrast. If multiple interactions occur in the same detection “granule”, the described analysis will fail to identify them separately, so a single interaction will be delivered as a combination of those interactions. The overall event will not be as reliable for Compton imaging, and if the combined interactions are found at the first or second Compton scattering, which are very important to correctly determine the order of the interactions, and the scattering angle, the event will contribute to image noise, unless discriminated upon. These events are named *scrambled events*.

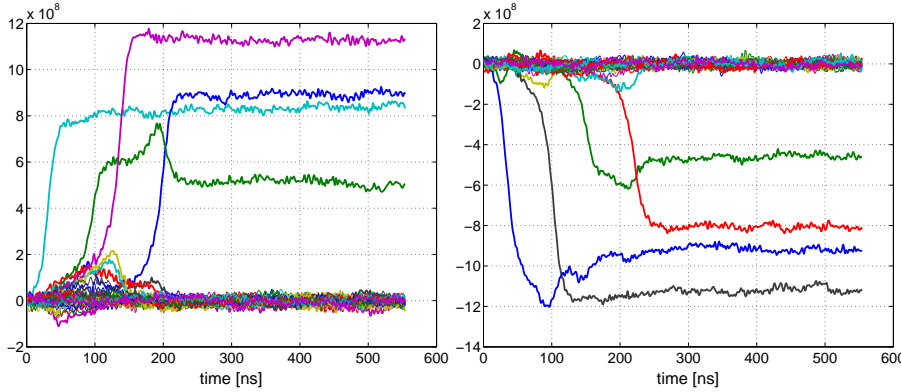


Fig. 6. Simulated signals of a 600keV γ -ray interacting 4 times in a virtual planar Ge detector with orthogonal strips. Left: AC side, right: DC side

The figure 7 depicts an example showing how the interactions occurring in a simulated event are reconstructed using the described PSA and CES.

4.3 Gamma-ray tracking

Having provided the list of interactions by CES, the aim of the *Gamma-ray tracking* module is to determine the γ -ray scattering sequence in the detector. An accurate determination of the scattering sequence is the single most important factor to determine the quality of the final imaging result. For each event, the γ -ray tracking algorithm will have to provide the scattering angle,

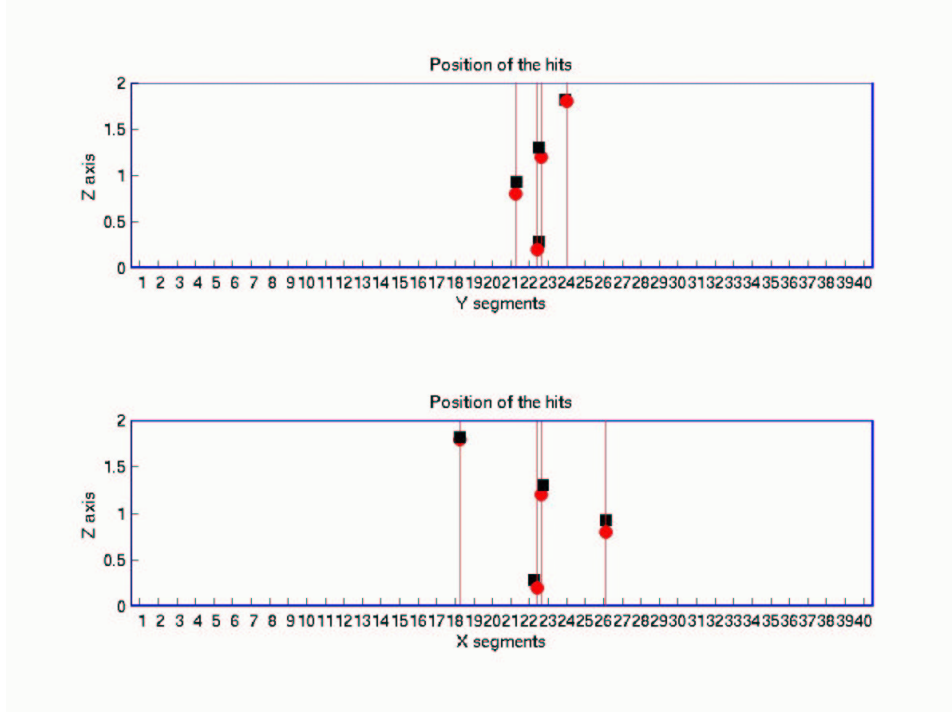


Fig. 7. The positions of 4 interactions taking place in a virtual planar Ge detector with orthogonal strips (circles: simulated vertices, squares: vertices identified by the PSA-CES algorithms).

the scattering direction and the vertex of the first Compton scattering. These factors will be used to reconstruct the image of γ -ray sources. Along with these parameters, the estimated angular uncertainty ($\delta\theta$) and the Figure of Merit for tracking (FoM_{track}) will be also provided for each reconstructed γ -ray photon. These two numbers will be very important in the decision of using the photon associated to them for imaging. Depending on the type of application, the threshold in these numbers to select imageable photons will vary. For example, if the aim of the imager is to decrease the detectability threshold of a compact source in a complex radioactive environment, a certain combination of the FoM_{track} and $\delta\theta$ will offer the smallest minimum detectable activity for such a compact source. If however, the aim is to achieve an image of the highest possible contrast or best resolution, a different set of thresholds will be required. Ultimately, gamma-ray tracking can be used with the only aim of selecting the photons that appear to have had full energy deposition in the detector, in this way improving the spectroscopic peak-to-background ratio (P/B). Many recent studies were conducted in the nuclear spectroscopy field in this direction [14]. There is a significant difference between the present problem and those studies in the sense that unlike in those cases, when the focus was on decomposing multiple gamma-ray photons occurring at the same time in the detection system, in our imaging application, the focus is on reconstructing a photon at a time.

There are two different tracking algorithms, one applies to events of only two

interactions, the other applies to events of three or more interactions. For two interactions, when the energy deposited in the photoelectric effect (second interaction) is bigger than the energy released in a Compton backscattering for the incident photon, only one scattering sequence is possible. Besides this case, it is not possible to use kinematics arguments to find the most probable scattering sequence for two interactions. For the situation where the scattering sequence is ambiguous, statistical arguments can be used. A tracking figure of merit can be calculated for each of the two possible sequences to take into consideration the probability for the photon to arrive to the first point of interaction through the detection material without being absorbed in a photoelectric effect $P_{\vec{r}_1}$, the probability to be scattered at the calculated scattering angle $P_{\cos\theta_1}$, and then, to arrive to the second point of interaction without being absorbed $P_{\vec{r}_{12}}$:

$$FoM_{N=2} = P(\cos\theta_1|E_0, E_1) = P_{\vec{r}_1} \cdot P_{\cos\theta_1} \cdot P_{\vec{r}_{12}} \quad (15)$$

The first and the third probability terms of the right side of the equation are calculated from $P_{\vec{r}_1} = \exp(-l(E_0) \cdot d_{min})$ and $P_{\vec{r}_{12}} = \exp(-l(E_0 - E_1) \cdot r_{12})$ respectively. l is the total mean free path for the incident photon of energy E_0 , d_{min} is the minimum distance a photon has to go through Ge to get to the point of interaction \vec{r}_1 , E_1 is the energy released in the Compton interaction, and r_{12} is the distance between the first and the second interaction. The second term involves the Klein-Nishina formula: $P_{\cos\theta_1} \sim (E_0 - E_1)/E_0 + E_0/(E_0 - E_1) - 1 + \cos\theta_1^2$.

For events of three or more interactions, besides the statistical factors, one can employ kinematics to find the most probable scattering sequence. This is possible because, for the intermediate interaction points, the scattering angle as measured from the relative positions of the interactions can be compared with the scattering angle as calculated from the Compton scattering formula. This procedure, however, gives good results only when the scattering angle can be accurately calculated, which requires a precise measurement of the photon energy at the time of the interaction, and of the energy released in that particular interaction. For this to happen, there are two necessary requirements: a.) the positions provided by the previous analysis steps should correspond to the real interactions; b.) the photon has to be totally absorbed in the detector, so that the sum of the energies of the subsequent interactions equals the energy of the down-scattered photon;

If these two conditions are not fulfilled, false scattering data are inferred, contributing to image noise. Some of these incompletely absorbed and scrambled events will be characterized by a smaller tracking FoM_{track} than the average FoM_{track} values obtained for viable, fully absorbed events. This makes it possible to reject some of these nuisance events by setting a threshold in the best value for the tracking FoM low enough to keep most good events, but high

enough to reject partially absorbed events and scrambled events. The position of the threshold will be determined by the requirements of the particular applications.

For each possible scattering sequence combination, the figure of merit is calculated as:

$$FoM_{N \geq 3} = P(\cos \theta_1 | E_0, E_1) \frac{1}{1 + \left(\frac{\chi^2}{M}\right)^E} \quad (16)$$

The definition of $FoM_{N \geq 3}$ contains the χ^2 term calculated as:

$$\chi^2 = \sum_{n=2}^{N-1} \frac{W_n}{N-1} \left(\frac{\theta_n - \theta_n^{(c)}}{\delta \theta_n^{(c)}} \right)^2 \quad (17)$$

Here, N is the total number of interactions, the $\theta_n^{(c)}$ is the calculated scattering angle using the Compton scattering formula for each intermediate interaction point of index n , θ_n is the scattering angle as measured from the relative position of the interaction points, and W_n is a weight factor associated with each interaction point that can be chosen to represent the intended importance of that particular interaction. We have assumed $W_n = 1$ for $n = 2 : N - 1$.

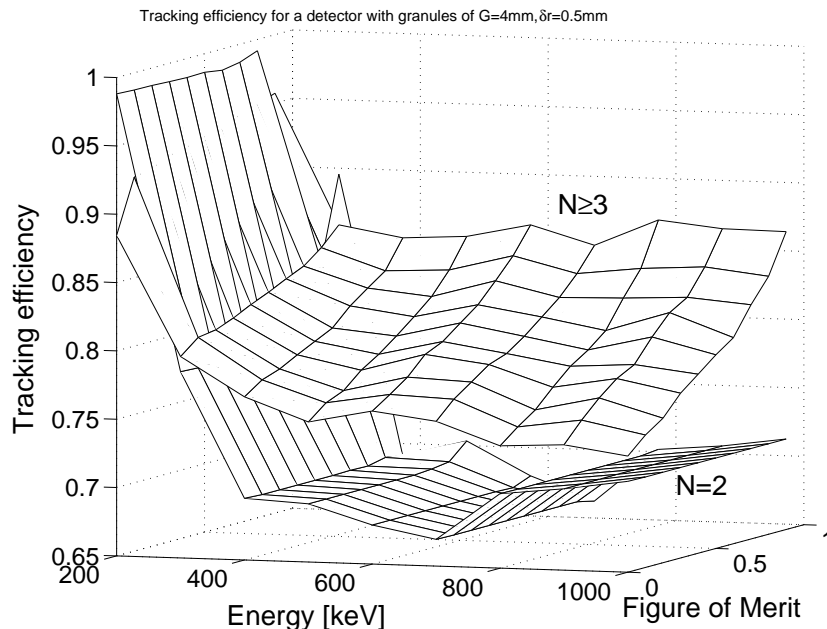


Fig. 8. Tracking efficiency obtained from Monte Carlo simulated events as function of the tracking figure of merit and gamma-ray energy. The 2 surface plots represents the cases for events of $N=2$ and $N \geq 3$ number of interactions.

Figures 8 and 9 are showing the tracking efficiency calculated as the fraction of events reconstructed correctly out of the number of events assumed correct

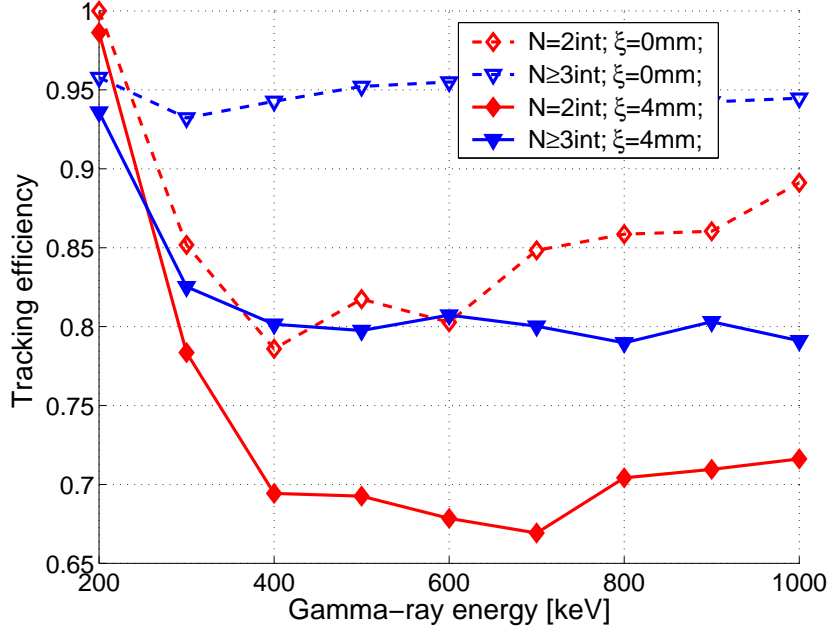


Fig. 9. Tracking efficiency for events of $N=2$ and $N\geq 3$ number of interactions, as obtained in a Ge detector containing "granules" of $G=0\text{mm}$ and $G=4\text{mm}$ (Monte Carlo simulated events). The selected events were chosen to have a tracking Figure-of-Merit above 0.5.

by the γ -ray tracking algorithm. The events were obtained by Monte Carlo simulations using GEANT4 library [13]. Figure 8 shows the variation of the tracking efficiency with the tracking figure-of-merit FoM_{track} and γ -ray energy E_0 , assuming a detector granularity of $g=1.62$ ($\xi = 4\text{mm}$). In figure 9, the tracking efficiency is represented for the cases when the granularity, g , is zero and 1.62, for events of 2 interactions and 3 or more interactions. Energy resolutions typical for a Ge detector were used. The effect of the Compton profile in Ge was also considered.

4.4 Image reconstruction

Since first proposed by Todd et al. [1], Compton cameras posed a great challenge in what regards image reconstruction due to the geometric particularity of their "projections". Unlike the tomographic imaging systems, where line-projections are easily reconstructed using either binned or list-mode data, employing iterative or analytic interversions, Compton cameras produce cones of various orientations, openings, resolutions, positions, which make binning of data very unpractical due to the huge parameter space. There have been several works studying various analytical reconstruction methods [17–19], some of them however, requiring various restraining conditions. To this date, no specific analytical algorithm seems to have gained a popular acceptance. Most of

the previous studies on Compton cameras have opted for various implementations of the iterative method of Maximum Likelihood (ML) [20]. For the purpose of assessing the basic capabilities of SPEIR, this is also the reconstruction method of choice in this work. Here, a simple list-mode implementation of the iterative algorithm was employed, with its iterative steps:

$$\lambda_l^{(s)} = \lambda_l^{(s-1)} \sum_{j(\cap l)} \frac{k_{lj}}{\sum_{i(\cap j)} k_{ij} \lambda_i^{(s-1)}} \quad (18)$$

$\lambda_l^{(s)}$ is the amplitude of the pixel l (voxel in 3D) at the iteration s , $\lambda_l^{(s-1)}$ is the amplitude of the same pixel at the precedent iteration. The main sum $\sum j(\cap l)$ is over all the events j whose cones intersect pixel l , k_{lj} is the weight with which pixel l contributes to event j , the sum at the denominator is over all pixels i intersected by the cone of event j , k_{ij} is the weight with which pixels i contribute to event j . An example of a reconstructed image using

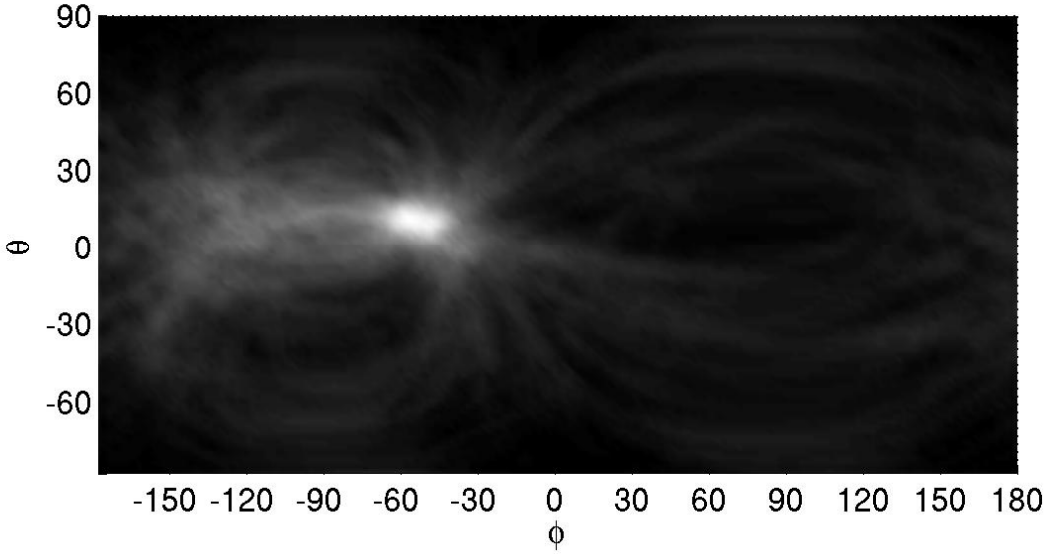


Fig. 10. Two ^{22}Na sources as appearing in the image produced by back-projecting the Compton cones

this ML implementation is shown in figure 11. For comparison purposes, the figure 10 shows the image map at iteration number 0 obtained by simply back-projecting the Compton cones onto the sky-map. The image is made out of two ^{22}Na point-like sources 15° apart. Although the two sources can not be observed independently from each other in the raw picture obtained by back-projecting the Compton cones, they become evident already after 6 iterations. The image shown in figure 11 was obtained in 15 iterations. The events included in the reconstruction were selected to have an estimated maximum angular uncertainty of 5° . The same angular uncertainty of 5° is found in the final reconstructed image.

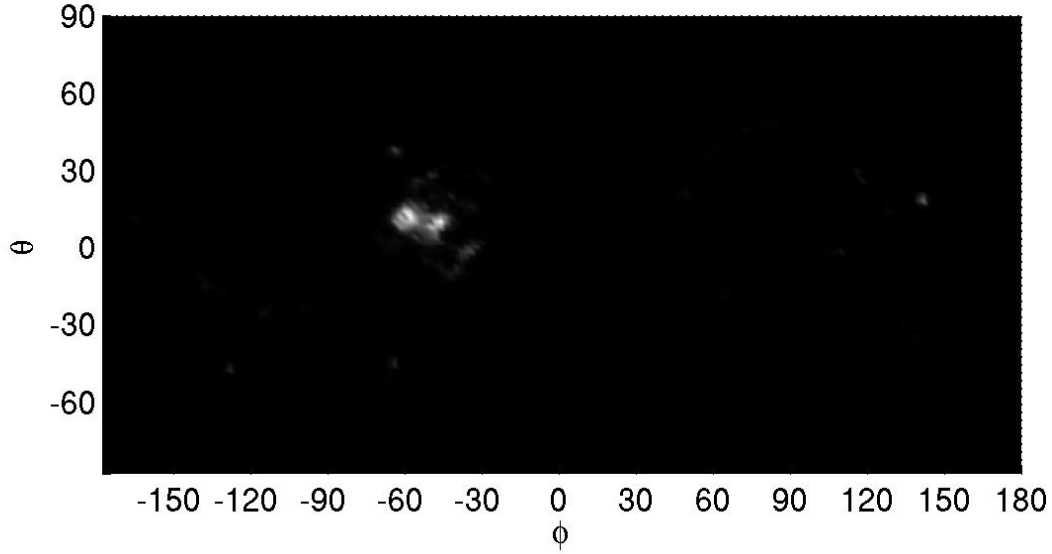


Fig. 11. Two ^{22}Na sources as appearing in the Maximum Likelihood reconstructed image (iteration no. 15)



Fig. 12. Panoramic image in the laboratory showing the superposed contour plot of the 511keV γ -ray sources

In a separate experiment, the panoramic *TotalViewTM* photolens camera was used in conjunction with SPEIR to demonstrate the capability of the system to visually identify the γ -ray sources. Figure 12 shows an example of a panoramic image on top of which the contour plot of a part of the γ -ray map (over a certain threshold) is superposed. The photons selected for imaging were in an energy window around 511keV. In the next figure (fig. 13), a zoomed region from the panoramic image containing a ^{22}Na source is shown.

5 Conclusions

A first prototype of a Compton imager was made using planar Ge detectors with orthogonal strips. Analysis techniques have been developed to reconstruct

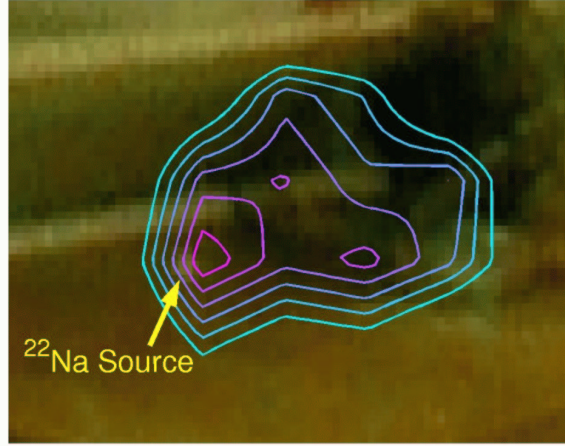


Fig. 13. Zoomed-in image of the ^{22}Na source

the scattering sequence of gamma-ray photons in a position sensitive detector, and to efficiently extract the information relevant for imaging the source of the incoming photons by using the Compton scatter principles. The developed methods have been implemented in a detection system using a single position sensitive planar Ge detector with orthogonal strips. The measurement results indicate an efficient use of the gamma-ray photons for Compton scatter imaging, even for higher resolution constraints assumed on the reconstructed image.

We expect that systems based on this design will be of interest for various applications, ranging from nuclear medicine, nuclear non-proliferation and environmental monitoring to gamma-ray astrophysics. This prototype system will be tested as-is as a demonstration unit for nuclear non-proliferation and environmental monitoring applications. Its usefulness as a scanner for small animal SPECT will be also pursued. In this respect, lighter radionuclides which emit gamma-rays of energies higher than 1MeV can be investigated as new SPECT tracers. Among them, ^{14}O , ^{24}Na (found in extra-cellular fluids), ^{43}K (found in cells), ^{47}Ca , ^{28}Mg , ^{52}Mn , ^{59}Fe , ^{55}Co , ^{56}Co could open new lines of research in biomedical investigations.

Acknowledgements

The authors would like to acknowledge Klaus Zioc for making detector available. This work was performed under the auspices of the U.S. Department of Energy by University of California, Lawrence Livermore National Laboratory under Contract W-7405-Eng-48. This investigation was supported by Laboratory Directed Research and Development program under the project 03-LW-031.

References

- [1] R.W. Todd, J.M. Nightingale and D.B. Everett, “A proposed γ camera”, *Nature*, 251, p.132-134, 1974.
- [2] V. Schönfelder, A. Hirner and K. Schneider, “A Telescope for Soft Gamma Ray Astronomy”, *Nucl. Instr. and Meth. in Phys. Res.*, 107, p. 385-394, 1973.
- [3] J.W. LeBlanc et al., “C-SPRINT: A Prototype Compton Camera System For Low Energy Gamma Ray Imaging” *IEEE Trans. on Nucl. Sci.*, 45, no.3, pp.943-949, 1998;
- [4] V. Schönfelder, et al., “The Imaging Compton Telescope COMPTEL on the Gamma-Ray Observatory”, *IEEE Trans. on Nuclear Science*, NS-31, 766-770, 1984.
- [5] V. Schönfelder et al., “Instrument Description and Performance of the Imaging Gamma-Ray Telescope COMPTEL aboard the COMPTON Gamma-Ray Observatory”, *Astrophys. J. Suppl.* 86, pp.657-692, 1993.
- [6] Hull, E.L. et al., *SPIE Proceedings*, Bellingham Washington, 4507, 2001.
- [7] Luke, P.N., Madden, N.W., Rossington, C.S., Wesela, M., *IEEE Trans. Nucl. Sci.*, 39, 590, 1992.
- [8] R. Ribberfors, *Phys. Rev. B* 12, p.2067, 1975.
- [9] D. Brusa et al., *Nucl. Instr. Meth. Phys. Res. A*, Vol. 379, pp. 167-175, 1996.
- [10] F. Biggs, L.B. Mendelsohn, J.B. Mann, *Atom. Data Nucl. Data Tables* 16, 1975.
- [11] Y.F. Du, Z. He, G.F. Knoll, D.K. Wehe, W. Li, *Nucl. Instr. Meth. Phys. Res. A*, Vol. 457, pp. 203-211, 2001.
- [12] C.M. Davisson and R.D. Evans, “Gamma-Ray Absorption Coefficients”, *Reviews of Modern Physics*, Vol. 24, No. 2, 1952.
- [13] S. Agostinelliae, J. Allison, K. Amako et al. GEANT4—a simulation toolkit, *Nucl. Instr. Meth. A*, Volume 506, Issue 3, p. 250-303, 2003
- [14] Schmid, G.J. et al., *Nucl. Instr. Meth. A*, Vol. 430 (1) pp. 69-83, 1999.
- [15] A. Georgiev and W. Gast, *IEEE Trans. Nucl. Sci.*, 40, No. 4, 770, 1993.
- [16] S. Amrose, S. E. Boggs, W. Coburn, R. P. Lin and D. M. Smith “Calibration of 3D positioning in a Ge cross-strip detector”, *Nucl. Instr. Meth. in Phys. Res. A*, 505, p.170-173
- [17] R. Basko, G.L. Zeng and G.T. Gullberg, “Application of spherical harmonics to image reconstruction for the Compton camera”, *Physics in Medicine and Biology*, 43, pp.887-894, 1998.
- [18] L.C. Parra, “Reconstruction of cone-beam projections from Compton scattered data”, *IEEE Trans. Nucl. Sci.*, NS47, p.1543-1550, 2000.

- [19] T. Tomitami and M. Hirasawa, "Image reconstruction from limited angle Compton camera data", *Physics in Medicine and Biology*, 47, p.2129-2145, 2002.
- [20] S.J. Wilderman, W.L. Rogers, G.F. Knoll and J.C. Engdahl, "Fast Algorithm for List Mode Back-Projection of Compton Scatter Camera Data", *IEEE Trans. Nucl. Sci.*, NS45, p.957-962, 1998.
- [21] Boggs, S.E. and Jean, P., *Astron. & Astroph. Suppl.*, 145, p.311, 2000.
- [22] Kroeger, R.A. et al., *Proc. of the IEEE NSS/MIC San Diego*, N4-4, 2001.
- [23] J.D. Kurfess, *IEEE Transactions on Nuclear Science*, 45, no.3, pp.936-942 (1998);
- [24] J.D. Kurfess, 5th Compton Symposium, Portsmouth, New Hampshire, AIP Conference Proceedings, (1999); ESA SP-382, pp.591-598 (1997);